Advanced and versatile interferometric technique for the characterization of photonic integrated devices

Luis A. Bru,[1] ⓘ Daniel Pastor,[1,*] and Pascual Muñoz[1,2]

[1]*Photonics Research Labs, ITEAM, Universitat Politècnica de València, c/ Camino de Vera s/n, Valencia 46022, Spain*
[2]*VLC Photonics S.L., c/ Camino de Vera s/n, 46021 Valencia, Spain*
*[*dpastor@dcom.upv.es](mailto:dpastor@dcom.upv.es)

Abstract: Adaptable and complex optical characterization of photonic integrated devices, permitting to unearth possible design and fabrication errors in the different workflow steps are highly desired in the community. Here, we propose a technique capable of resolving full optical amplitude and phase response, in both frequency and time domains, of a photonic integrated device. It relies on optical frequency domain interferometry and makes use of a novel integrated architecture; a 3-way interferometer enabling single input and single output detection. We derive the test structure design rules and provide extensive experimental validation in silicon nitride and silicon on insulator technologies, by testing relevant devices such as arrayed waveguide grating, Mach-Zehnder interferometers, and ring resonators. Horizontal and vertical chip coupling, different external setup arrangements, and the optical dispersion de-embedding inherent to the technique are demonstrated. Finally, we discuss why this characterization approach might lay the groundwork of a standard testing tool for photonic integrated devices.

1. Introduction

Unstoppable technological improvements in Photonic Integrated circuits (PICs) are making them to become actual mature technologies which find applications in diverse fields such as tele/datacom, bio sciences, sensing, automotive, etc. where silicon on insulator (SOI), silicon nitride (SiN) and indium phosphide (InP) have established as the principal photonic integration platforms [1–3]. In the complex process of PIC manufacturing, thorough characterization of integrated waveguides and devices becomes essential to speed up production, optimize designs and reduce costs. Prevailing laboratory characterization setups, e.g. formed by broadband light source and optical spectrum analyzer (OSA), provide amplitude spectral response of the device under test (DUT). This is a valuable information, albeit not always enough to satisfy a rigorous test of complex devices, which is enabled by the characterization of the DUT optical phase response.

The techniques based on interferometry allow to track the DUT phase response and therefore, through processing, to switch between frequency and time domains of the DUT response. The different interferometric techniques can be classified, broadly speaking, by whether they are carried out in the time domain or in the frequency domain [4,5]. Amongst them, optical time domain reflectometry (OTDR) [6,7] is a well-known technique that requires short light pulse generation and achieves high length ranges, suitable in the world of optical fiber testing and devices; OTDR has a phase-sensitive version [8]. Low-coherence interferometry (LCI) [9,10] makes use of broadband light sources and involves moving mechanical parts in the body of the interferometer, achieving great spatial resolutions desirable in optical sensing. Optical frequency domain reflectometry technique (OFDR) manages without those difficulties, being based on a passive interferometric setup and by relying on a tunable laser source (TLS) which determines

a relatively high spatial resolution. These characteristics makes OFDR an appealing testing and characterization technique in the context of integrated devices [11]. Once the time domain response is obtained, the events taking place in the DUT can be identified and analyzed. Intended DUTs can be designed as well to apply techniques which allow to assess key optical parameters [12,13]. OFDR stands for reflectometry, inherited from its former application in the field of optical fibers, though the same apparatus can be also set in transmission mode as it is case in the present work. We make use of OFDI acronym, standing for interferometry, for the sake of generality.

The integration of an OFDI architecture has been previously proposed [14], where the interferometric part is co-integrated along with an arrayed waveguide grating (AWG) as a DUT in a SiN platform, proving OFDI capabilities. Additionally, it was demonstrated an inherent dispersion de-embedding mechanism as a direct consequence of using the same integrated waveguide cross-sections for the DUT and the delay arms of the interferometers. In the direction of considering it as a functional test structure, the main practical inconvenient is the requirement of two output optical ports. The proposed technique in this work relies on a novel integrated architecture, a three-way Mach-Zender interferometer (3-MZI), which presents single optical input and single optical output detection and keeps the same virtues as the proposed in [14]. (very preliminary work of this was communicated in conferences [15,16]). We describe in detail the functioning of the technique in section 2, by providing the theoretical framework which justifies the novel architecture and allows to set their design rules. We detail how, with an additional processing step, the necessary traces to do OFDI are decoupled from the super-interferogram resulting from the 3-MZI. Thereafter, experimental proof and analysis of different DUTs in two different technologies is provided in section 3: an AWG in a SiN platform and MZIs and ring resonators (RR) in a SOI platform. Beyond, we also demonstrate the versatility of the technique in the light source and detection parts: apart from the conventional TLS plus photodetectors arrangement to do OFDI, we make use of a typical photonics laboratory bundle formed by a broadband source (based in amplified spontaneous emission, ASE) and an OSA, an unprecedented approach to the best of our knowledge and enabled by the use of integrated interferometric structures, as we shall argue. Finally, in section 4, we draw our conclusions and discuss the technique potential for the integrated photonics community.

2. Interferometric technique

In Fig. 1, a sketch of the whole physical implementation related to the technique is shown. In the center of figure is the proposed integrated test structure, the passive 3-way MZI, integrated on-chip with the DUT inserted in the shortest arm. The other two paths are the delay arms, implemented by integrated spirals. As aforementioned, a super-interferogram is obtained after measurement, and condenses all the necessary information to carry out OFDI processing. With the proper design of the 3-MZI lengths, that we describe in what follows, a processing step allows to decouple the required traces to apply OFDI processing. Regarding the external setup, i.e. the light source and photodetection part, we consider two different arrangements, A1 and A2, for which we give more details in section 3, including the actual equipment used in this work.

2.1. OFDI with integrated waveguides

OFDI is the underlying engine in the technique proposed in this work. OFDI is a well-known interferometric technique able to provide the optical amplitude and phase response of a DUT in frequency and time domains [17–19]. It relies on homodyne detection, enabling fast wavelength scanning: the light source is programmed to sweep a given band $\Delta\lambda = \lambda_2 - \lambda_1$, centered at λ_0, so the signal is split to simultaneously feed two interferometers (usually MZIs). In the first MZI, with path length difference (PLD) given by ΔL, the DUT is inserted in one of the arms (DUT-MZI), whereas the other (TRIG-MZI) has a PLD given by $\Delta L' > \Delta L$. After the
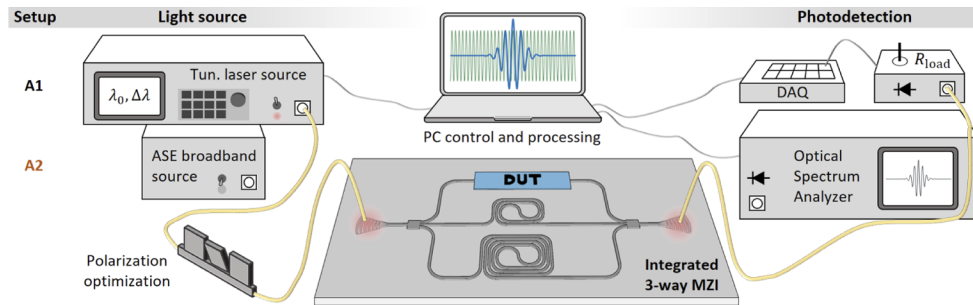
Fig. 1. Sketch of the physical implementation of the technique: there are two different arrangements A1 and A2 for the light source and photodetection part. In the center, the integrated test structure, a 3-way MZI with the DUT in one of the arms, that is accessed by a single input and single output scheme.

wavelength-resolved scanning, interferograms are generated in such a way that the TRIG-MZI fringes track the possible phase distortion coming from the sweep scanning nonlinearities, as it does the DUT-MZI ones added to the phase response of the DUT. A core step so-called linearization is then executed, where the TRIG fringes trigger the DUT ones so that the common phases recorded by both interferograms are cancelled out, resulting into a trace exempt from sweep non-linearities and linearly sampled in frequency, provided that chromatic dispersion of the TRIG-MZI waveguides (typically, optical fiber) can be neglected in the working band. There are two options to implement linearization: in a direct way, acquiring samples by electronically programming triggering the DUT interferogram when a condition in the TRIG fringes is met or indirectly, by acquiring first both interferograms at a higher sampling rate. We employ the latter in this work for convenience as it allows a full observation and control of the raw data. Nyquist criterion must be followed to avoid aliasing in the linearization process and this is related to the PLDs of the MZIs, that are connected to the free spectral range (FSR) of the interferograms as FSR $\simeq \lambda^2/(n_g \Delta L)$. In the direct acquiring approach it is customary to take one point per TRIG-MZI interferogram FSR to trigger the DUT, so Nyquist criterion leads to $\Delta L \le \Delta L'/2$ for all ΔL involving the DUT extent δL (i.e. the range $\{\Delta L - \delta L/2, \Delta L + \delta L/2\}$) in order to hold the DUT time domain response within the temporal semi-window of width $\Delta L'/2$. The complex time domain response of the DUT is retrieved, after linearization, by applying inverse fast Fourier transform (IFFT) algorithm. In this picture, the corresponding temporal events can be identified and their amplitude and phase analyzed. The amplitude events are represented by peaks, whose widths are fundamentally given by the span of the sweep and determine the ideal spatial resolution of the system $\delta z_{\text{id}} = \lambda_0^2/(n_{g,0} \Delta \lambda)$ ($n_{g,0}$ is the group index in the center of the band), although the peaks experience an added widening in the more realistic case of dispersive waveguides [17]. Temporal crop windows can be designed by the user that delimit a selection of the temporal contributions of interest, to then apply Fast Fourier Transform (FFT) to obtain the coresoponding spectral reconstruction. This feature is useful to get a rid of any undesired contribution in the spectrum visualization, provided that its temporal position is different from the ones of interest.

The external OFDI setup interferometric part is typically formed by optical fiber. It has been extensively used to analyze optical fiber devices such as complex Bragg gratings, where prevails the reflectometry mode that can be enabled by the employment of an optical circulator when using MZIs (e.g. see Ref. [18]), or also using other types of interferometers (e.g. Michelson [17]). More recently, OFDI has been increasingly utilized to test integrated devices [20–22] and the transmission mode, easily implemented with MZIs, is commonly utilized depending on the specific application or device [12,13], as it is the case in this work. The integration of the

interferometric part along with the DUT can be considered in the quest of an advanced integrated test structure. In comparison to the external approach, the employment of integrated waveguides gives some advantages: they provide incomparable accuracy to tailor small MZI PLDs permitting to tight the temporal window and implying larger interferogram FSRs which opens the way for less demanding light source and photodetection parts in terms of resolution (e.g. basic laboratory equipment as ASE and OSA, as we demonstrate in this work). Integrated waveguides are also more stable propagating media against external conditions, improving reliability and repeatability of the measurements. On the other hand, they are also typically very dispersive media, something typically undesired in OFDI since it limits the spatial resolution of the system. However, as detailed in [14], in the singular case where the same or similar waveguides are employed for the DUT and the MZIs arms, the corresponding acquired phases in the interferograms are cancelled in the linearization part, including the phase contributions due to the presence of dispersion, which gives rise to an inherent dispersion de-embedding mechanism.

2.2. *Integrated test structure*

We make some assumptions about the waveguides for the sake of simplicity, in order to describe analytically the integrated test structure: we assume a single-mode regime with absence of polarization rotation, and a maintained light source and waveguide coherence along the involved lengths. Moreover, we also consider fully transparent waveguides with negligible loss, as well as the power splitters or couplers working ideally, in the considered bands and lengths. Let us consider a technology platform where optical propagation through the routing waveguides is described by the propagation constant $\beta(\lambda)$. In the 3-MZI, we define L_2 and L_3 as the corresponding lengths for the delay arms, whose propagation is represented by the phase terms $\exp(i\beta L_2)$ and $\exp(i\beta L_3)$, respectively. The short arm, with average path length L_1 such that $L_1 < L_2 < L_3$, is composed of routing waveguide plus the DUT, which gets described by its transfer function $H(\lambda) = |H(\lambda)| \exp(i\phi(\lambda))$ where its spectral phase response is represented by $\phi(\lambda)$. At the output of the 3-MZI, the resulting optical field is the superposition $A = H(\lambda)\exp(i\beta L_1) + \exp(i\beta L_2) + \exp(i\beta L_3)$ so that the corresponding optical intensity can be expressed as $I = |A|^2 = I_{DC} + I_{AC}$, where the AC term is, after some algebra:

$$I_{AC} = \cos(\beta' \Delta L') + H(\lambda)(\cos(\beta' \Delta L) + \cos(\beta' \Delta L_{add})), \tag{1}$$

i.e. the oscillatory part of the superinterferogram is composed of 3 contributions, one of them corresponding to a conventional MZI with PLD given by $\Delta L' = L_3 - L_2$, and the remaining two carry the DUT transfer function at $\Delta L = L_2 - L_1$ and $\Delta L_{add} = L_3 - L_1$. These ones turn into a cluster of contributions when the DUT is considered to be composed by a group $H(\lambda) = \sum H_i(\lambda)$ covering a spatial region of width δL. In this case, there also appears an additional AC group of terms from $|H(\lambda)| = H^*H$, the DUT self-beatings, spanning along the $\{0, \delta L\}$ range (see Fig. 2). Therefore, the AC term of the superinterferogram condenses the OFDI interferograms superimposed at the combination of paths given by ΔL and $\Delta L'$, in addition to contributions replicating DUT information that we shall discard.

In order to recover DUT and TRIG interferograms, a pre-processing step is required: it consists in apply IFFT to the detected super-interferogram $I(\lambda)$, indentify the contributions of interest (at ΔL and $\Delta L'$ impulsive positions) and define crop windows to separately isolate them. Next step is to apply FFT to them and trace the real part so that the phase information gets tracked by the common sinusoides. The retrieved spectra correspond with the OFDI desired interferograms which contain essentially the same features as if they were measured separately, as done in [14], including the whole phase information of the DUT, sampling in wavelength, chromatic dispersion and scanning nonlinearities. Accidentally, thanks to the full isolation when applying the crop windows in the pre-processing step, I_{DC} and any vestige of spurious events placed at different impulsive positions than the PLD of the interferograms themselves is filtered out. To carry out
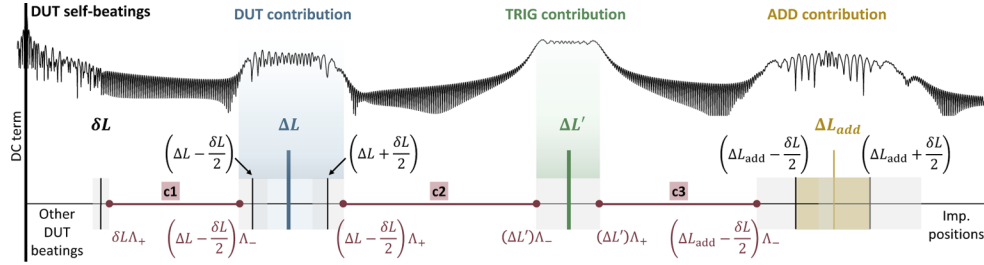
Fig. 2. Schematic picture of the impulsive response of the super-interferogram: the different contributions are expected to appear at their impulsive positions, each of them with a given width. The non-overlapping conditions c1, c2 and c3 are imposed by choosing a given gap distance (thick red line) between these contributions.

this pre-processing, the involved waveguide lengths L_1, L_2 and L_3 must be chosen in such a way that the expected contributions do not overlap in the impulsive domain, by controlling c1, c2 and c3 distance conditions represented in Fig. 2. Due to the fact that almost all commercial light source plus photodetection solutions in photonics provide a sampling in wavelength (as the two we employ for the experiment), the detected super-interferogram is nonlinearly sampled in frequencies. This feature, together with the presence of chromatic dispersion in the waveguides, leads to an additional broadening for each contribution in the impulsive domain such that if its corresponding impulsive position is x, it occupies a range $\{x\Lambda_-, x\Lambda_+\}$ where $\Lambda_\pm \equiv 1 \pm B'_\lambda$ and $B'_\lambda = B_\lambda (1 + \chi)$, being $B_\lambda = \Delta\lambda/\lambda_0$ the fractional bandwidth. We define a dispersion coefficient $\chi = -\lambda_0 cD/2n_{g,0}$, where D is the group velocity dispersion parameter and c the speed of light in vacuum (see section 1 in Supplement 1). By imposing the non-overlapping conditions, i.e. the c1–c3 distances highlighted in thick red line in Fig. 2 to be greater than a safety distance sx, along with the Nyquist criterion required to do OFDI and stating $\Delta L'/2 - (\delta L/2 + sx) \geq \Delta L \geq \delta L/2 + sx$, after some inspection the following design rules can be established:

- Consider the shortest possible DUT arm average length L_1, being the minimum and maximum involved lengths $L_1 \pm \delta L/2$. Consider the wavelength conditions as well, through $\Lambda \equiv \Lambda_+/\Lambda_- = 1 + \delta\Lambda$, being $\delta\Lambda = 2B'_\lambda/(1 - B'_\lambda)$.

- $L_{2,\min} = L_1 + (1.5 + \delta\Lambda)\,\delta L + (1 + 0.5\delta\Lambda)\,sx + \Theta(\mathbf{P})\mathbf{P}$, so that we establish $L_2 = L_{2,\min} + \delta L_2$ in accordance with the tolerances of the real design.

- Finally, $L_{3,\min} = 3L_2 - 2L_1 + 2sx + \delta L$,

where Θ is the Heaviside step function and the polynomial $\mathbf{P} = \mathbf{C}^{-1}((\mathbf{A})\delta L + (\mathbf{B})sx)$, being $\mathbf{A} = B'^2_\lambda + 8B'_\lambda - 1$, $\mathbf{B} = -4B'_\lambda(B'_\lambda - 2)$ and $\mathbf{C} = 5B'^2_\lambda - 6B'_\lambda + 1$. Since each impulsive contribution has a fundamental non-zero width due to the limited bandwidth (determining δz_{id}, as explained above), the safety distance sx should be chosen to be at least twice δz_{id} to prevent contributions overlapping. However in the real world, depending on the utilized wavelength scanning mechanism, there exists the possibility of some degree of nonlinearity on it. This turns into an added phase distortion in the super-interferogram that, similarly as it occurs with the aforementioned nonlinear frequency sampling, increases the broadening of the impulsive contributions. This effect is observed in this work and covered in more detail in section 2 of Supplement 1, together with a detailed derivation of the design rules.
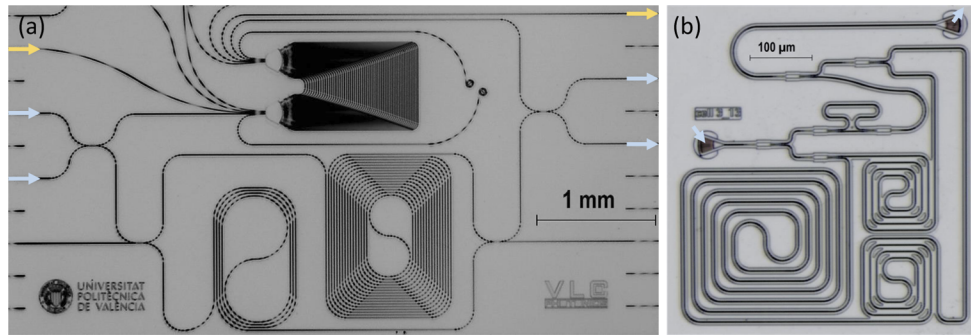
Fig. 3. Microscopy picture of the 3-MZI test structures: (a) SiN with the AWG, and (b) SOI with a $\Delta l = 200\mu$m MZI, as DUTs.

3. Experimental work

The employed experimental setup is composed of the light source and photodetection parts, which together are in charge of performing a wavelength scanning for a given band. As shown in Fig. 1, we make use of two different approaches: on the one hand, arrangement A1 corresponds to the equipment that is customary in OFDI, a TLS source performing the wavelength scanning and a photodetector plus a data acquisition card (DAQ) to digitize optical detected signal. For this setup, we employ a Yenista TUNICs T100R providing 10 mW reliable source in the C-band (1490-1650 nm) with hop-free continuous scannings up to 100 nm/s, and Thorlabs FGA01FC InGaAs photodiodes mounted in a standard high impedance front-end without electronic amplification, providing an electrical voltage proportional to the optical intensity. This signal is digitized by the DAQ, a National Instruments USB-6259 ready to acquired 16-channel at 1 MS/s aggregated rate. On the other hand, we make use of an alternative approach A2, interesting since it makes use of other common laboratory equipment: it employs an ASE broadband source (NP Photonics C and L Band ASE, 19 dBm integrated power in the 1525-1610 nm band) and an OSA (Yokogawa AQ6370C, 0.02 nm resolution) in the photodetection part, which plays the wavelength scanning role. The OSA limited resolution is sufficient in this context thanks to the small PLDs which can be tailored in the integrated MZIs, giving rise to spectral FSRs easy to resolve.

3.1. AWG in SiN

Experimental validation of the technique is provided employing an AWG as a DUT on a chip that was fabricated on CNM-VLC silicon nitride platform. In the measured die, a Si_3N_4 waveguide layer of 280 nm height is deposited by low pressure chemical vapor deposition (LPCVD) onto a 2.5 μm SiO_2 buffer, and covered by a 2.0 μm SiO_2 cladding by plasma-enhanced chemical vapor deposition (PECVD) [20,23]. The single-mode waveguides employed for routing are quasi-rectangular 1 μm width designed for central wavelength $\lambda = 1550$ nm. Input/output light coupling to the chip is carried out by horizontal coupling making use of adiabatic tapers for better mode size matching. The fabricated device includes a 5×5 channel AWG with 59 waveguides in the array and an FSR of 32 nm (4 THz), as shown in Fig. 3(a). The central input and output channels of the AWG are routed directly to input/output (left and right) facets of the chip (yellow arrows in the figure), aimed to be tested with external setup. A neighboring combination of input/output channels of the AWG is connected to the 3-MZI: light is coupled through one of the inputs (blue arrows at left), reaching a 50:50, 2×2 multimode interferometer (MMI) that splits the signal in power. The upper output of the MMI is routed to the AWG and the bottom one is split again to feed the two delays lines implemented by spirals. All the paths are conveniently put together again by means of MMIs, so that the resulting beating signal is collected at one of the

outputs. Not shown in Fig. 3(a) at the top is a similar 3-MZI device accessing the AWG with the complementary input/output channel combination and with a different arrangement of the MMIs. The lengths of the different paths are chosen to overtake the minimum requirements imposed by the design rules derived above, to ensure the experimental validation: the AWG has a spatial widht of $\delta L \simeq 2.285$ mm and its average path in the 3-MZI is $L_1 = 6.756$ mm, so that the spirals lenghts in the other paths are determined such that $\Delta L \simeq 10.039$ mm and $\Delta L' \simeq 34.998$ mm (see section 2 of Supplement 1 for more details).
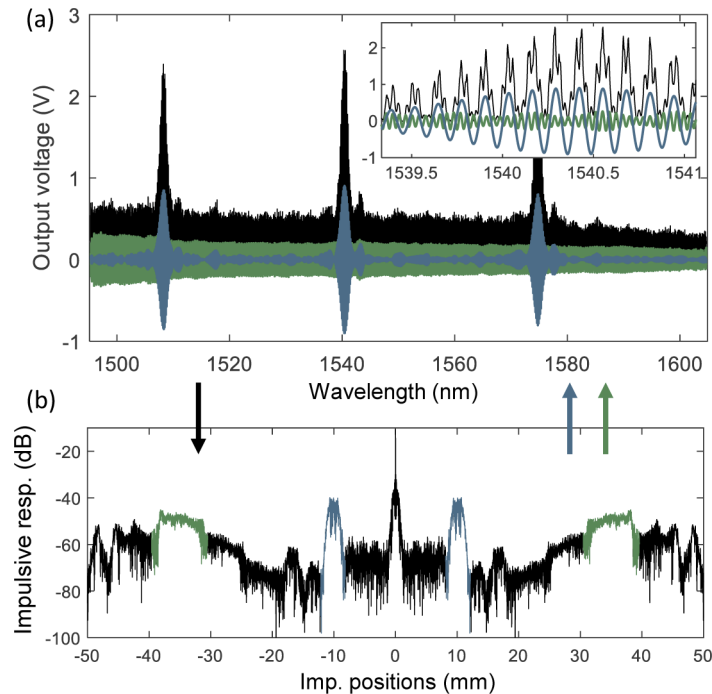

Fig. 4. Super-interferogram processing to decouple DUT and REF interferograms. (a) In black line, the recorded super-interferogram and the recovered DUT and TRIG interferograms in blue and green lines, respectively. In the inset, a zoom around the $\lambda = 1540$ nm region. In (b), the obtained impulsive domain where the DUT and TRIG contributions are highlighted correspondingly.

The measurements of the 3-MZI test structure are performed with both A1 and A2 arrangements previously described and shown in Fig. 1. As done in previous work [14], the average group index can be retrieved from the OFDI measurements by computing the TRIG interferogram number of interferometric oscillations N in the working band $\Delta\lambda$, applying $n_{g,0} = (\lambda_1\lambda_2N)/(\Delta\lambda\Delta L')$, and resulting in this case $n_{g,0} = 1.8245 \pm 0.0015$. In Fig. 4, a measurement performed with A1 setup and the corresponding pre-processing is shown. In (a), the obtained super-interferogram is shown in black curve for a sweep scanning of $\Delta\lambda = 109$ nm around $\lambda_0 = 1550$ nm. After applying the IFFT algorithm, the impulsive domain is obtained and its amplitude represented in (b), showing the expected symmetry with the DC contribution in the center and the different expected contributions around. Among them, the broadened contributions corresponding to the DUT (blue curve) and TRIG (green curve) interferograms are straighforwardly identified, then isolated by defining squared crop windows (i.e. filling with zeros everything else around) to finally, separately, apply FFT back to the frequency domain to recover the interferograms. In the inset, a zoom in the $\lambda = 1540$ nm region shows clearly how the structure of the super-interferogram is successfully decoupled into the two interferograms. Let the reader notice that both DUT and

TRIG interferograms appear at a lower level, with a marked symmetry around the *x*-axis: this is because the super-interferogram DC contribution is intentionally not included in the definition of the crop windows, along with any other contributions placed at different impulsive positions, resulting into smooth interferogram traces.

After OFDI processing of the obtained interferograms, the time domain response of the AWG is obtained and its amplitude is shown in Fig. 5(a), in black line. The *x*-axis is expressed in positions and it can be referred to as spatial domain too. Indeed, due to the dispersion de-embedding mechanism, the broadening of the temporal peaks, which is a temporal effect, is removed and thus it is strictly correct to refer to this picture as such. The train of consecutive peaks represents each path followed by light through the array waveguides, with an spacing which corresponds to the designed one $\delta l = 39.4$ µm. The expected Gaussian envelope as a consequence of the free space propagation in the AWG slabs is perfectly observed. A simple Gaussian fitting is applied to the peaks in order to get an estimation of the spatial resolution by computing the full width at half maximum (FWHM). By analyzing the 15 central contributions and average over 10 measurement takes, the obtained spatial resolution is $\delta z_{exp,A1} = 12.6 \pm 0.2$ µm, which is pretty close the ideal one $\delta z_{id,A1} = 12.1$ µm. The device is also measured employing A2 arrangement, for which the band $\Delta\lambda = 95$ nm centered at $\lambda_0 = 1562.5$ nm is considered. In this case, even though the ASE source presents a non-uniform spectral shape, the trace is normalized to the source by subtracting a reference measurement (i.e. propagation through a straight waveguide) to it. The obtained time domain amplitude is represented by an orange curve in Fig. 5(a), again reproducing the expected pattern. Same analysis of the peaks estimates $\delta z_{exp,A2} = 16.5 \pm 0.8$ µm in this case, standing for the reduced bandwidth of the ASE source, for which the ideal spatial resolution is $\delta z_{id,A2} = 14.1$ µm. In both A1 and A2 experiments, thanks to the dispersion de-embedding mechanism the obtained spatial resolution tends to the ideal one, permitting to directly observe and analyze nearby temporal contributions of the DUT, something which otherwise turns complicated (e.g. when measuring with an external OFDI system, see Ref. [14]), due to the high chromatic dispersion of the integrated waveguides.
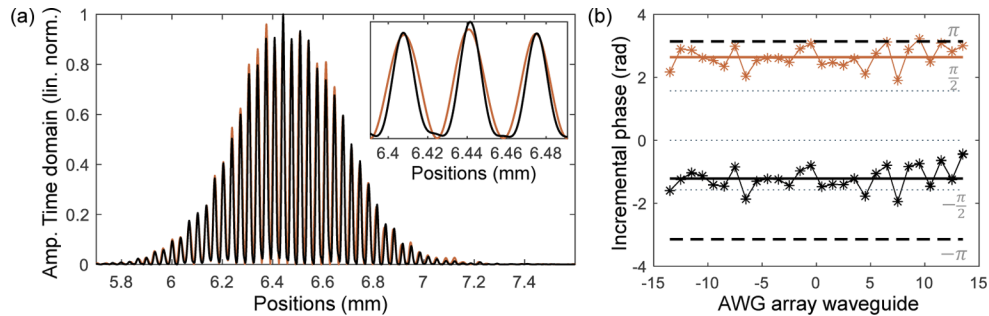

Fig. 5. (a) Amplitude time domain response of the AWG, normalized in linear scale. A zoom in the inset shows the detail of the temporal contributions in the AWG central region. (b) Incremental optical phase between the 29 central waveguides of the AWG. In black line, the obtained trace with A1 arrangement, whereas the orange line corresponds to A2.

The time domain response provides also the phase response of the DUT. Apart from $\phi(\lambda)$, in practice the trace also contains an absolute phase component that varies from one take to another, which makes not straightforward to assess absolute optical phases [24]. Nonetheless, this does not prevent us to assess incremental phase between the different contributions inside one measurement take. In Fig. 5(b), the incremental phase between the 29 central contributions is shown for A1 and A2 arrangements, in black and orange lines, respectively. The averaged incremental phase over 10 takes in the case of A1 is around -1.21 rad with a standard deviation of 0.37 rad, while for A2 measurement is performed for one take and shows a great agreement

with the former (standard deviation of 0.36 rad), observing some divergence only for the outer analyzed peaks of the AWG. The ideal functioning of the AWG relies on the generation of a linear phase response between the waveguides in the array, such that the incremental phase is a constant. The magnitude of the variations around this value is signature of the phase errors in the arrayed waveguides, and consequently the deviation from the ideal behaviour of the AWG which mainly manifests by the appearance of strong secondary lobes [25].

By applying FFT to the time domain response, the spectral response of the AWG is recovered and shown in Fig. 6 at the top, for the A1 and A2 arrangements (in black and orange line, respectively). Both traces coincide almost perfectly and show an AWG with a well-defined spectral response, presenting secondary lobes at about 15-20 dB below the main one, which in turn shows the expected shape. These traces are in perfect accordance with the external OSA take, shown at the bottom of the figure. Since this is measured by accesing the AWG throughout the external input/output combination (yellow arrows in Fig. 3), a frequency shift is observed accordingly. The same design of AWG, fabricated in a previous run of the same technology, was tested in previous work [14] and found to have considerably stronger incremental phase errors (deviations in the order of 3 rad), what explained the strong secondary lobes in its spectrum. In this case, probably due to some fabrication optimization, the AWG has an improved performance which is in accordance with the evaluated incremental phase variation.
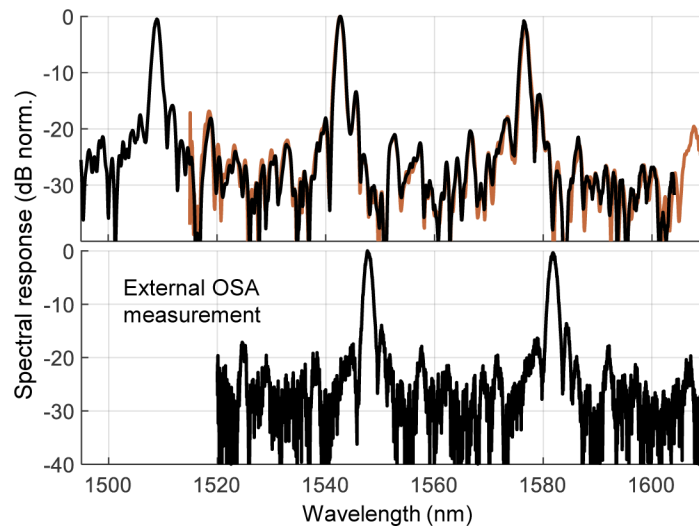

Fig. 6. Spectrum of the AWG normalized in dB scale. At the top, the spectral reconstructions are shown in black and orange lines for A1 and A2 arrangement measurements, respectively. At the bottom, the spectral measurement of the AWG external input/output with OSA.

3.2. RRs and MZIs in SOI

Some different 3-MZI test structure devices involving RRs and MZIs as DUTs were designed to be fabricated in Inphotech SOI technology platform [26], where the employed deep-etched cross-section is a rectangular waveguide of 480 nm width and 220 nm height designed to be single-mode at λ = 1550 nm, and patterned by electron beam lithography (EBL). In this technology, the expected propagation loss is α_{SOI} = 3 dB/cm and the recommended minimum bending radius is around 10 μm. Due to the limited stitching area cells, characteristic of EBL, the design of the test structure units were optimized to stick to a small footprint of just 0.5×0.5 mm^2. In Fig. 3(b), a microscopy picture of one of the test structure cells is shown, where chip optical input/output (blue arrows) is conducted vertically by the use of grating couplers (GC), the

circuitry delay lines are implemented by three spiral structures and the DUT shown is a MZI with PLD equal to 200 μm. The different paths are divided and join where it is required by employing 1x2 MMIs.

The vertical coupling is of particular interest since it is indispensable for wafer scale testing of waveguides and devices, highly desired as it enables technology performance monitoring in intermediate steps of the PIC fabrication process.
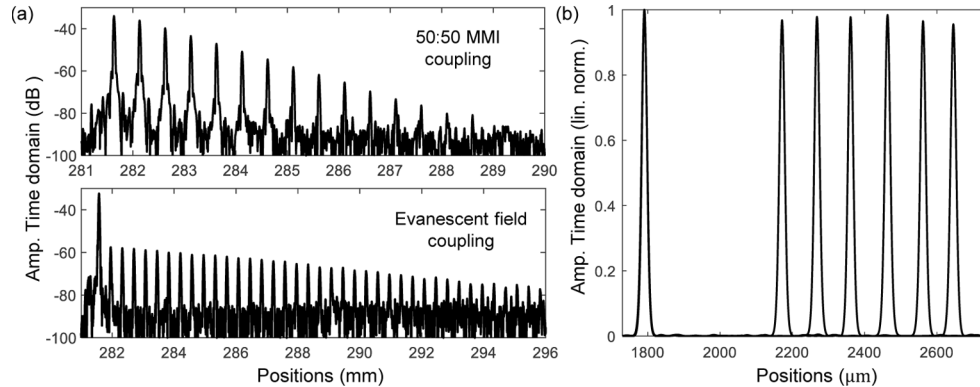

Fig. 7. (a) Amplitude time domain response in dB scale of the measured RRs. The measurements are performed with external OFDI setup; for the 50:50 MMI coupled RR above, and for the evanescent coupled RR below. (b) Amplitude time domain response normalized in linear scale of the measured MZIs. The contributions correspond to the 6 different PLD cases, each of them composed of two peaks.

However, the GCs are TE mode filtering and have limited bandwidth. Since we are not implementing a polarization diversity characterization system, TE mode filtering does not entail an issue. Considering the limited bandwidth, a processing step in the OFDI processing consists in applying an apodization window to the DUT interferogram in order to reduce secondary lobes of the peaks when switching to the time domain (at the cost of a reduced effective wavelength span, which in turn decreases the spatial resolution [17]). The smoothly decaying fashion of the GC bandwidth curve can be considered as a partial implementation of the apodization window, so that it implements this processing step in a natural way. In the present case, the coupling efficiency presents a Gaussian-like apodization window of about 45 nm centered at $\lambda_0 = 1570$ nm, so that we set up the TLS to sweep $\Delta\lambda = 160$ nm around λ_0 in the measurements, in order to properly resolve this window.

An extremely important device to be utilized as DUT is the RR: these devices have been extensively utilized for a myriad of PIC applications. In general, the design of RRs is tricky because their performance involves delicate optical phenomena like evanescent coupling, birefringence or waveguide chromatic dispersion [27,28]. Therefore, in order to optimize designs, a thorough characterization of these devices turns essential. Beyond, RRs can be used as a test structure that, together with OFDI technique, provide a technology multi-parameter characterization platform [12]: the time domain response of the RR consists of a train of power decaying contributions corresponding to the light roundtrips in the RR, containing information about the RR coupling conditions, roundtrip loss and dispersion, and polarization effects such as, for instance, fundamental TE/TM mode coupling when using single-mode waveguides. Some RR models were included in the present SOI chip, both standalone and as DUT in 3-MZI structures. Unfortunately, the considerations about the DUT spatial width δL (i.e. the number of resolvable roundtrips) turned out to be insufficient when setting the delay path lengths L_2 and L_3 in the 3-MZI structure, so overlapping of contributions in the impulsive domain and aliasing occurs. We have

measured standalone RRs though with an external OFDI setup, and the resulting amplitude time domain response is shown in Fig. 7(a) for a RR coupled by 50:50 MMI with 150 μm roundtrip length at the top, and for an evanescent field coupled RR with 150 μm roundtrip length too, and a waveguide gap distance of 170 nm. The expected decaying power train of pulses is perfectly visualized in both cases. For the MMI coupled RR, up to 14 pulses are well-observed over the noise floor, with a constant slope (in dB scale) which includes the first-to-second peak power ratio, as expected when having $\kappa \simeq 0.5$ for the RR light coupling. In the case of the evanescent coupled RR, the first contribution is considerably more powerful standing for a weaker RR coupling, whereas a greater number of contributions with a flatter decay is visualized, signature of a higher Q factor RR. With the correct design, all this information can be also retrieved by the technique suggested in this manuscript.

Other DUTs which have been included to be tested in the 3-MZI test structures are MZIs. Specifically, 6 MZIs with different PLDs in the range $\Delta l = \{200, 250, \ldots, 450\}$ μm. The resulting amplitude time domain responses, after all the processing, are shown together in Fig. 7(b). The first peak at the left accumulates the different cases short arm of the MZI, whereas it can be perfectly checked how the separation of the remaining peaks increases by the designed step of 50 μm. In all the cases, the first peak is the one which carries more power while the second peak is slightly lowered. A subtle power decay can be noted between the peaks of the second group, standing for the accumulated propagation loss when the 50:50 performance of the MMIs can be assumed. As it happens with RRs, MZIs are very important devices diversely utilized in a broad range of applications in PICs, including in the context of characterization. For example, as it can be intuited from their amplitude time domain response, they can be used to design test structures which, together with OFDI technique, allows to obtain both waveguide properties (e.g. propagation loss and group index) and power splitting ratio of optical couplers like MMIs [13]. In the context of OFDI and thus, the technique described in this article, MZIs and other type of interferometers can be also used to test active elements in a technology as, for example, thermal tuners (something that was not possible to implement in the present multi-project run). The incremental phase between different temporal contributions can be calculated as done in previous subsection. In an interferometer, the increments of this calculated phase when tuning the active elements provide a mean to characterize the power needed to carry out a π-shift when a MZI is employed as an optical switch, or the thermal crosstalk when the active element is placed anywhere outside the device. The same idea can be applied to test more complex devices such as tunable Sagnac loop interferometer based reflectors [29].

4. Perspective and conclusions

In this work, we have proposed an interferometric technique to characterize photonic integrated devices in amplitude and phase, both in frequency and time domains. Relying on OFDI, in the heart of the technique is a novel integrated test structure, a 3-MZI holding the DUT in one of its arms, which generates a super-interferogram condensing all the necessary information to proceed with OFDI in a single input and single output measurement scheme. This approach addresses the major issue of the direct implementation of an integrated OFDI from a practical point of view [14], and still keeps the virtues of using integrated waveguides to build the interferometers: they are stable propagation media that adapt to the DUT dimensions and characteristics that, amongst other advantages, have allowed to demonstrate OFDI for more limited wavelength resolution systems as the common laboratory equipment formed by a broadband ASE source in the C-band and an OSA performing the wavelength scanning. Moreover, their use leads to an inherent dispersion de-embedding mechanism that allows to keep the spatial resolution of the system to the ideal one, given by the scanning bandwidth.

The 3-MZI has been described, derived their design rules, and explained the associated processing to decouple the OFDI interferogram: the super-interferogram is transformed to

its impulsive domain, where the contributions corresponding to the different 3-MZI path combinations appear at their impulsive positions. A set of non-overlapping conditions, together with sampling Nyquist criterion, give rise to the design rules of the 3-MZI arms lengths. Then, DUT and TRIG contributions can be isolated and transformed back to the frequency domain. A varied experimental validation of the technique has been provided by testing an AWG in a SiN platform and MZIs in a SOI platform. In the case of the SOI platform, RRs were included as well but incorrectly designed, so OFDI measurements of the standalone RRs has been measured and shown, as an example of what the technique could have allowed to resolve. It is fairly remarkable the demonstration of the technique involving chip vertical coupling (by means of GCs) since it is the way to optically access the chip on a wafer-scale level. This scenario is much desired in the PIC community as it brings the opportunity to anticipate chip performance from critical fabrication steps, incorporating in-line photonic testing.

Further refinements in the design of the 3-MZI structures may be considered in the future. We find specially relevant those allowing to restrict the devices footprint. On the one hand, in the linearization part (the DUT resampling by the TRIG), we have considered the common OFDI approach: the set of sampling points is given by the 'increasing' zeros of the TRIG interferogram sinusoid. There is room to improve this part by considering to double the number of sampling points from the TRIG, by including the 'decreasing' zeros as well. It is straightforward to implement in the processing and, when considered in the design, it involves a factor 1/2 in the Nyquist condition. This leads to more relaxed lengths of the delay paths (L_2 and L_3), resulting into shorter spirals and thus, better optical power conditions and a significant reduction of the test structure footprint. On the other hand, if several DUTs want to be tested, it can be considered to share delay paths between them, although the use of optical switches turns required. A passive strategy to address this is to connect the considered DUTs serially in the DUT path of the 3-MZI. This would result into a half number of delay paths (when considering two DUTs), as desired, but at the cost of being considerably longer to fulfill the design rules with the multi-DUT. In our opinion, the proposed technique meets a great deal of virtues in terms of versatility and advanced characterization to become a fundamental tool for PIC testing. And also, to be combined with applications which has been proposed (based on OFDI) to obtain important parameters about a given technology [12,13,21]. Furthermore, compact integrated test cells such as the one in Fig. 3(b), could become the photonic equivalent of the CMOS electronics test structures, that are usually placed in the chip scribe line areas of the reticles, aimed at process step performance monitoring.

Disclosures. The authors declare no conflicts of interest.

Data availability. No data were generated or analyzed in the presented research.

Supplemental document. See Supplement 1 for supporting content.

References

1. P. Muñoz, P. W. L. van Dijk, D. Geuzebroek, M. Geiselmann, C. Domínguez, A. Stassen, J. D. Doménech, M. Zervas, A. Leinse, C. G. H. Roeloffzen, B. Gargallo, R. Baños, J. Fernández, G. M. Cabanes, L. A. Bru, and D. Pastor, "Foundry developments toward silicon nitride photonics from visible to the mid-infrared," IEEE J. Sel. Top. Quantum Electron. **25**, 1–13 (2019).
2. M. Smit, K. Williams, and J. van der Tol, "Past, present, and future of INP-based photonic integration," APL Photonics **4**(5), 050901 (2019).

3. X. Chen, M. M. Milosevic, S. Stankovic, S. Reynolds, T. D. Bucio, K. Li, D. J. Thomson, F. Gardes, and G. T. Reed, "The emergence of silicon photonics as a flexible technology platform," Proc. IEEE **106**(12), 2101–2116 (2018).

4. X. Bao, W. Li, Z. Qin, and L. Chen, OTDR and OFDR for distributed multi-parameter sensing, in *Smart Sensor Phenomena, Technology, Networks, and Systems Integration 2014*, vol. 9062 W. Ecke, K. J. Peters, N. G. Meyendorf, and T. E. Matikas, eds., International Society for Optics and Photonics (SPIE, 2014), pp. 1–11.

5. K. Yuksel, M. Wuilpart, V. Moeyaert, and P. Megret, Optical frequency domain reflectometry: a review, *2009 11th International Conference on Transparent Optical Networks*, pp.1–5, (2009

6. P. Healey, R. C. Booth, B. E. Daymond-John, and B. K. Nayar, "Otdr in single-mode fibre at 1.5 um using homodyne detection," Electron. Lett. **20**(9), 360–362 (1984).

7. S. Stopiński, K. Anders, S. Szostak, and R. Piramidowicz, Optical time domain reflectometer based on application specific photonic integrated circuit, in *2019 Conference on Lasers and Electro-Optics Europe and European Quantum Electronics Conference*, (Optical Society of America, 2019), pp. ch–p–38.

8. R. Zinsou, X. Liu, Y. Wang, J. Zhang, Y. Wang, and B. Jin, "Recent progress in the performance enhancement of phase-sensitive otdr vibration sensing systems," Sensors **19**(7), 1709 (2019).

9. A. F. Fercher, W. Drexler, C. K. Hitzenberger, and T. Lasser, "Optical coherence tomography - principles and applications," Rep. Prog. Phys. **66**(2), 239–303 (2003).

10. D. Derickson, Fiber optics test and measurement (Prentice Hall, 1998).

11. L. A. Bru, B. Gargallo, G. Micó, R. Baños, J. D. Doménech, A. M. Sánchez, R. Mas, E. Pardo, D. Pastor, and P. Muñoz, Optical frequency domain reflectometry applied to photonic integrated circuits, in *18th European Conference on Integrated Optics (ECIO)*, (Warsav, 2016), pp. o–08.

12. L. A. Bru, Z. Ye, D. Pastor, and P. Muñoz, Multi-parameter estimation of high-Q silicon rich nitride resonators using optical frequency domain reflectometry, in *Integrated Optics: Devices, Materials, and Technologies XXII*, vol. 10535 International Society for Optics and Photonics (SPIE, 2018), pp. 148–155.

13. L. A. Bru, D. Pastor, and P. Muñoz, "On the characterization of integrated power splitters and waveguide losses using optical frequency domain interferometry," in *21st European Conference on Integrated Optics (ECIO)*, (Ghent, 2019), p. W.Po1.25.

14. L. A. Bru, D. Pastor, and P. Muñoz, "Integrated optical frequency domain reflectometry device for characterization of complex integrated devices," Opt. Express **26**(23), 30000–30008 (2018).

15. L. A. Bru, D. Pastor, B. Gargallo, D. Doménech, C. Domínguez, and P. Muñoz, Advanced integrated testing engine towards a complete characterization of photonic integrated devices, in *2018 European Conference on Optical Communication (ECOC)*, (2018), p. SP3.MIC07.

16. L. A. Bru, D. Pastor, B. Gargallo, D. Doménech, C. Domínguez, and P. Muñoz, Advanced integrated testing engine towards a complete characterization of photonic integrated devices, in *20th European Conference on Integrated Optics (ECIO)*, (Valencia, 2018), p. We.3.A.4.

17. U. Glombitza and E. Brinkmeyer, "Coherent frequency-domain reflectometry for characterization of single-mode integrated-optical waveguides," J. Lightwave Technol. **11**(8), 1377–1384 (1993).

18. B. J. Soller, D. K. Gifford, M. S. Wolfe, and M. E. Froggatt, "High resolution optical frequency domain reflectometry for characterization of components and assemblies," Opt. Express **13**(2), 666–674 (2005).

19. D. K. Gifford, B. J. Soller, M. S. Wolfe, and M. E. Froggatt, "Optical vector network analyzer for single-scan measurements of loss, group delay, and polarization mode dispersion," Appl. Opt. **44**(34), 7282–7286 (2005).

20. P. Muñoz, G. Micó, L. A. Bru, D. Pastor, D. Pérez, J. D. Doménech, J. Fernández, R. Baños, B. Gargallo, R. Alemany, A. M. Sánchez, J. M. Cirera, R. Mas, and C. Domínguez, "Silicon nitride photonic integration platforms for visible, near-infrared and mid-infrared applications," Sensors **17**(9), 2088 (2017).

21. F. Morichetti, A. Canciamilla, C. Ferrari, M. Torregiani, A. Melloni, and M. Martinelli, "Roughness induced backscattering in optical silicon waveguides," Phys. Rev. Lett. **104**(3), 033902 (2010).

22. D. Zhao, D. Pustakhod, K. Williams, and X. Leijtens, "High resolution optical frequency domain reflectometry for analyzing intra-chip reflections," IEEE Photonics Technol. Lett. **29**(16), 1379–1382 (2017).

23. Silicon nitride photonic integration platform, http://www.imb-cnm.csic.es/index.php/en/clean-room/silicon-nitride-technology.

24. C. Caló, B. Robillart, Y. Gottesman, A. Fall, F. Lamare, K. Merghem, A. Martinez, A. Ramdane, and B. Bcnkelfat, Spectral and temporal phase measurement by optical frequency-domain reflectometry, *26th International Conference on Indium Phosphide and Related Materials (IPRM)*, pp.1–2, (2014

25. P. Munoz, D. Pastor, J. Capmany, and S. Sales, "Analytical and numerical analysis of phase and amplitude errors in the performance of arrayed waveguide gratings," IEEE J. Sel. Top. Quantum Electron. **8**(6), 1130–1141 (2002).

26. Inphotec silicon-on-insulator photonic integration platform, https://www.inphotec.it/technology_post_type/silicon-photonics-2/.

27. D. G. Rabus, Ring Resonators: Theory and Modeling (Springer Berlin Heidelberg, 2007) chap. 2, pp. 3–40.

28. W. Bogaerts, P. De Heyn, T. Van Vaerenbergh, K. De Vos, S. Kumar Selvaraja, T. Claes, P. Dumon, P. Bienstman, D. Van Thourhout, and R. Baets, "Silicon microring resonators," Laser & Photon. Rev. **6**(1), 47–73 (2012).

29. J. Fernández, L. A. Bru, D. Pastor, D. Doménech, C. Domínguez, and P. Muñoz, Universal tunable integrated mirror: the sagnac loop interferometer, in *XI Reunión Española de Optoelectrónica* (OPTOEL), (2019), pp. 1–3.